Journal of Alloys and Compounds 512 (2012) 199–206

Contents lists available at SciVerse ScienceDirect

Journal of Alloys and Compounds

journal homepage: www.elsevier.com/locate/jallcom

Interface characterization and atomic intermixing processes in Be/W bilayers deposited on Si(0 0 1) substrates with Fe buffer layers

V. Kuncser[a,*], P. Palade[a], G. Schinteie[a], S.G. Sandu[a], L. Trupina[a], G.A. Lungu[a], N.G. Gheorghe[a], C.M. Teodorescu[a], C. Porosnicu[b], I. Jepu[b], C.P. Lungu[b], G. Filoti[a]

[a] National Institute of Materials Physics, P.O. Box MG-7, 077125, Bucharest-Magurele, Romania
[b] National Institute for Laser, Plasma and Radiation Physics, P.O. Box MG-36, 077125, Bucharest-Magurele, Romania

ARTICLE INFO

Article history:
Received 25 July 2011
Received in revised form
19 September 2011
Accepted 20 September 2011
Available online 1 October 2011

Keywords:
PFCs
Be/W bilayers
Atomic inter-diffusion GIXRD
XRR
XPS
CEMS

ABSTRACT

Structural aspects and atomic intermixing processes in Be/W bilayers deposited on Si(0 0 1) substrates with Fe buffer layers enriched in the ^{57}Fe Mössbauer isotope have been studied via atomic force microscopy, grazing incidence X-ray diffractometry, X-ray reflectometry, X-ray photoelectron spectroscopy and conversion electron Mössbauer spectroscopy. The mentioned investigations allowed a full sequential characterization of the involved interfaces. Various ionic configurations appeared for Fe or W, while an amorphous state was observed in the case of Be.

It has been proven that the Be layer has a negative influence on the roughness of the whole structure, which however presents an oxidation gradient from more oxidized elements at the surface towards more reduced elements in deeper layers. A strong diffusion of the W atoms inside the Be layer, induced by the deposition method, as well as of the Fe atoms inside the Be layer, induced by thermal annealing, has been evidenced.

1. Introduction

The ambitious target of the current international programs for nuclear fusion is to demonstrate that in the next 30 years, the energy obtained by nuclear fusion can become a viable alternative from scientific, economic and safely exploitation point of view, to the needs for continuous growing energy consumptions. The envisaged way for promoting the nuclear fusion reaction is realized via an extremely hot plasma generated in a TOKAMAK torus, e.g. as in the case of the International Thermonuclear Experimental Reactor (ITER).

There are numerous important materials that must be successfully developed in order to make the thermonuclear reaction technologically viable [1,2], but, the most challenging task refers to the plasma facing components (PFCs) [3]. As it is known, in a TOKAMAK type reactor, the fusion takes place in extremely hot plasma, which is confined and kept away from the reactor walls or other material components through typical magnetic configurations, established by the so called limiters and diverters. In spite of the strong magnetic field confinement, the edge plasma exhausts heat and particle fluxes which finally lead to the erosion of the PFCs, by physical sputtering, chemical erosion or melting/sublimation, all these phenomena reducing the life time of the PFCs. On the other hand, the eroded atom-like impurities from the PFCs can migrate into the plasma core with negative influence on the fusion performances. Taking into account all the above mentioned aspects, the materials designed for the PFCs should have outstanding performances with respect to their thermo-mechanical properties, erosion yield, fuel retention capability, insignificant influence on the fusion performances and reduced activation. Unfortunately, the above requirements cannot be fulfilled by just one type of material, but by two distinct categories, each one with enhanced performances with respect to a complementary part of the requirements. Light elements, such as C or Be, with a low impact on the core plasma performances, have significant erosion yields whereas heavy elements such as W have a low erosion yield but can degrade strongly the plasma performances. Therefore, reduced activation Fe–9%Cr ferritic/martensitic steels and SiC/ceramic SiC composites covered by Be and/or W layers, in well defined sequences, can be considered for different PFCs. It is worth mentioning that another effect, related to the plasma wall interaction, consists in the fact that the sputtered atoms from PFCs can reach critical points of other components, as improper mixed compounds, which might affect their own performances. Hence, the knowledge of the atomic intermixing process and the related effect on structural and thermal properties of thin films and multilayers involving typical elements

* Corresponding author. Fax: +40 21 3690177.
E-mail addresses: kuncser@infim.ro, kuncser@yahoo.com (V. Kuncser).

0925-8388/$ – see front matter © 2011 Elsevier B.V. All rights reserved.
doi:10.1016/j.jallcom.2011.09.063

used in PFCs becomes of high importance, also in conformity with a complex international research program called Plasma Wall Interaction Task Force.

The present paper reports on a detailed study of structural aspects and atomic intermixing processes taking place in Be/W bilayers deposited on Si substrates with a thin Fe buffer layer partially enriched in the ^{57}Fe isotope, for an additional characterization of Si/Fe and Fe/Be interfaces, through the powerful method of ^{57}Fe Mössbauer spectroscopy. The main results, derived from Mössbauer spectroscopy and X-ray photoelectron spectroscopy (XPS), are corroborated with atomic force microscopy (AFM), grazing incidence X-ray diffractometry (GIXRD) and X-ray reflectometry (XRR) measurements.

2. Experimental details

The Fe tracer layers (4 nm thick), partially enriched in the ^{57}Fe Mössbauer isotope have been deposited either directly on a Si(0 0 1) substrate or on a polycrystalline W film (10 nm thick) previously grown on the Si(0 0 1) substrate. The samples were prepared by RF sputtering in Ar (10^{-2} mbar) at a power of 100 W, with the substrate kept at room temperature. The native Si oxide layer was not chemically removed from the substrate, but an etching process of 10 min was applied before deposition. The film thicknesses have been estimated from the deposition time, via a previous calibration, done on each type of material by growing thicker films and subsequent examination via reflected light total interference contrast microinterferometry. Nevertheless, in all cases, the thicknesses of the components of the final multilayer structure have been checked via X-ray reflectometry. An initial analysis of the thin Fe tracer layers by Mössbauer spectroscopy has shown that the films are almost completely oxidized due to the air exposure, inherent to changing the installation. Therefore, the RF sputtered Fe films were initially reduced in hydrogen atmosphere, prior to the Be deposition. A commercially available volumetric Sievert apparatus provided by Advanced Material Corporation, Pittsburgh, USA, has been used in this respect. The reaction with hydrogen has been done at 300 °C for 90 min under 10 bars H_2 pressure, after 20 subsequent cycles consisting of vacuum pumping and purging of hydrogen at lower temperatures (100–150 °C). According to our previous experience, the oxide reduction degree is very sensitive to the film thickness. While errors of at least 10% in this parameter are expected among subsequently obtained Fe films, their initial phase composition was analyzed by Mössbauer spectroscopy prior to any subsequent deposition. The intermixing at the Si/Fe and Fe/Be interfaces has to be considered by the analysis of sets of samples (before and after deposition, treatments, various processing, respectively). While the deposition of the Be films is subject to special regulations, the Be/W bilayers have been obtained in a special installation, using the thermionic vacuum arc (TVA) method, which is an original technology placed between electron beam evaporation and electrical vacuum arc discharge [4,5]. An electron beam can evaporate the material of interest, placed at the anode, as neutral particles which can be directly deposited on the substrate, placed at the cathode, for enough low electron energies and beam intensities. As soon as the anode potential overpasses a certain value, the evaporation rate increases as much as to allow an electrical discharge to be ignited in the gas formed by evaporation of the material intended to be deposited. By shifting between the two extreme regimes, pure, dense and well structured films of strongly variable thicknesses (from nanometers to micrometers) are grown in reasonable time intervals. By using many crucibles containing target materials as well as an increased number of electron guns, a range of complex multilayer structures involving binary and even ternary layered compositions can be obtained [6]. The method is very suitable for the deposition of Be based structures, from nanometer thickness (deserving studies related to the plasma wall interactions) to tenths of micrometers (e.g. for covering wall tiles). For the actual experiences, there have been grown on the reduced Fe tracer layers, Be(30 nm)/W(30 nm) bilayers, which were analyzed either as deposited or after a thermal annealing performed in vacuum at 600 °C, for 10 min. No bias was applied on the Si substrate during the deposition. The geometrical structure with nominal thicknesses of the components and the code of the considered layered samples, are resumed in the following:

WF: Si/W(10 nm)/Fe(4 nm), before the hydrogen reduction;
WFH: Si/W(10 nm)/Fe(4 nm), after hydrogen reduction;
F1: Si/Fe(4 nm), before the hydrogen reduction;
FH1: Si/Fe(4 nm), after hydrogen reduction.;
FH1BW: FH1/Be(30 nm)/W(30 nm);
FH1BWT: FH1BW after thermal annealing.

The atomic force microscopy (AFM) images have been obtained using a MFP-3D SA (Asylum Research) instrument working in intermittent contact mode at 0.5 Hz and with Si cantilevers (AC240TS, Olympus).

Both GIXRD and XRR have been performed with a Bruker type (D8 Advance) diffractometer working with Cu K_α radiation of 0.154 nm wavelength. The LAPTOS program has been used for fitting the XRR spectra whereas the qualitative analysis of the diffraction pattern has been performed via the EVA program.

The depth dependent XPS studies have been performed in a dedicated photo-emission vacuum room (SPECS GmbH) equipped with a Mg cathode emitting X-rays at 1253.6 eV and an electron analyzer of type Phoibos 150 mm with energy window of 50 eV and spectral resolution of 0.2 eV. Superficial charge effects have been compensated through a flood gun operating at 1 eV acceleration voltage and 0.1 mA electron current. The depth profile has been realized with a high intensity Ar^+ gun (IQE 12/38) generating a current of 10 μA at the sample surface, under an acceleration voltage of 5 kV. The investigated depth has been estimated via straightforward crystallographic considerations, by considering that each Ar^+ ion incident on the sample extracts only one atom from it.

Surface sensitive ^{57}Fe Conversion Electron Mössbauer Spectroscopy (CEMS) has been used to study the phase composition and the local structure of the Fe tracer layer as well as the interfacial mixing at the Si/Fe and Fe/Be interfaces. The spectra have been acquired at room temperature, in perpendicular geometry (with the gamma radiation perpendicular to the sample plane) with the sample placed in a home made gas flow proportional counter. The set-up involved a ^{57}Co source (Rh matrix) of 15 mCi activity and a spectrometer working with sinusoidal waveform. The NORMOS computer program by Brand [7] has been used for the least-squares fitting of the CEM spectra. The isomer shifts are reported relative to α-Fe at room temperature.

3. Results and discussion

According to our previous experience related to RF sputtering of very thin Fe films on Si substrates, the quality of the films can be much enhanced with respect to their crystalline structure, surface roughness and especially the lack of oxygen via a subsequent hydrogenation [8]. AFM pictures taken on samples WFH and FH1 are presented in Fig. 1. Both images evidence a tri-dimensional type of growth with formation of island-like morphologies which are larger on the Fe film deposited on the W buffer layer as compared to the case of the direct deposition on the Si(0 0 1) substrate. However, in spite of this difference, both samples present a root mean square (RMS) roughness of about 0.5 nm (a higher roughness of 1 nm was observed for the non hydrogenated samples WF and F1),

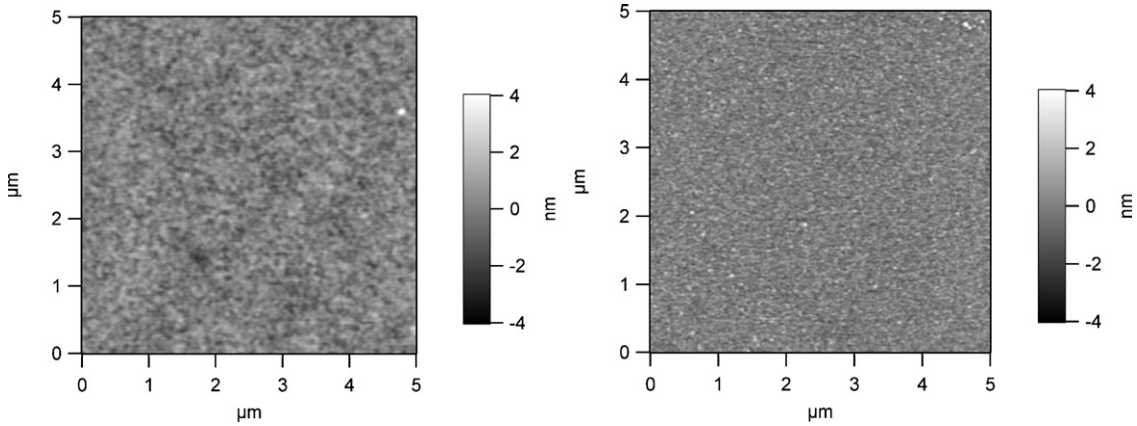

Fig. 1. AFM images taken on samples WFH (left side) and FH1 (right side).

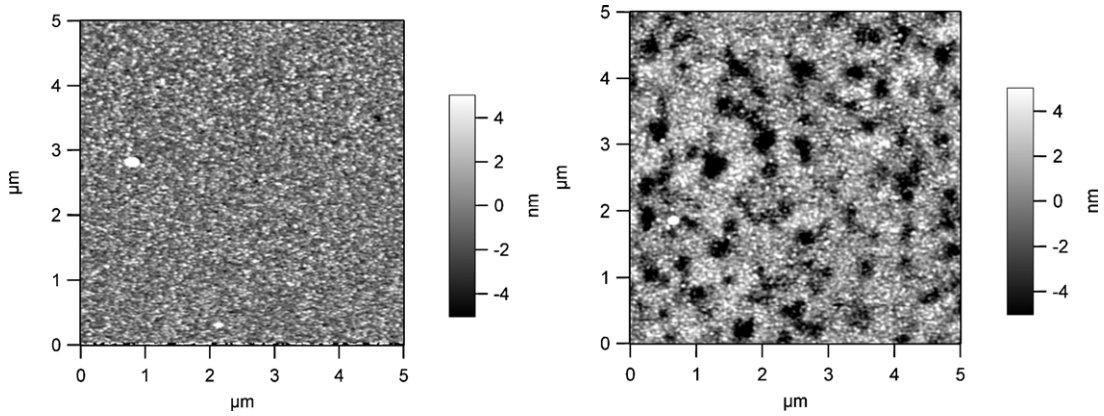

Fig. 2. AFM images taken on samples FH1BW (left side) and FH1BWT (right side).

proving the fact that films have formed already a continuous layer of a few nm thicknesses on the Si (or W) surface. Further on, the deposition of the Be/W additional layers have been processed only on the simplest structure of Si(0 0 1)/Fe. AFM images of the samples with additionally deposited Be/W bilayers, as deposited and after the thermal annealing (samples FH1BW and FH1BWT), are shown in Fig. 2.

It can be clearly seen that the surface roughness increases drastically as compared to the previous images (namely, at 2 nm as compared to initially 0.5 nm), most probably due to the Be film growing (Fig. 1 indicates that both Fe and W films showed a lower roughness). The annealed multilayer structure presents an even more irregular surface (2.6 nm roughness), with large and deep craters, proving that the upper layer of W can be drastically influenced by the Be underlayer, already subject to 600 °C thermal activation. Hence, the morphology, structure, density and related protective properties of a W layer can be intensely reduced by a Be underlayer.

No shaped GIXRD patterns have been observed on WFH and FH type samples, most probably due to the very low thickness and poor crystallization of films. However, the mass density profile of sample WFH obtained via XRR patterns (see Fig. 3) confirms the geometrical structure of the sample, Si/W(≈12 nm)/Fe(≈5 nm), as well as the relatively high roughness of the top Fe layer. The decrease of the Fe mass density gives a first hint about its possible strong oxidation.

The GIXRD patterns of the FH1BW and FH1BWT structures are presented in Fig. 4, (a) and (b), respectively. The inset of Fig. 4(b) shows a reference diffraction pattern corresponding to the Be target, which evidences a well crystallized structure of hexagonal Be with lattice parameters and intensity ratios very close to the theoretical values. At variance, none of the diffraction pattern of the FH1BW and FH1BWT multilayer samples evidenced the typical reflection planes of the hexagonal Be, but just reflection planes of two different tungsten phases, namely the simple cubic structure *Pm*-3*n*, with the lattice parameter approaching the theoretical value of 0.50 nm (noted by W1) and the body centered cubic (bcc) structure *Im*-3*m*, with the lattice parameter approaching the theoretical value of 0.316 nm (noted by W2). In spite of the very

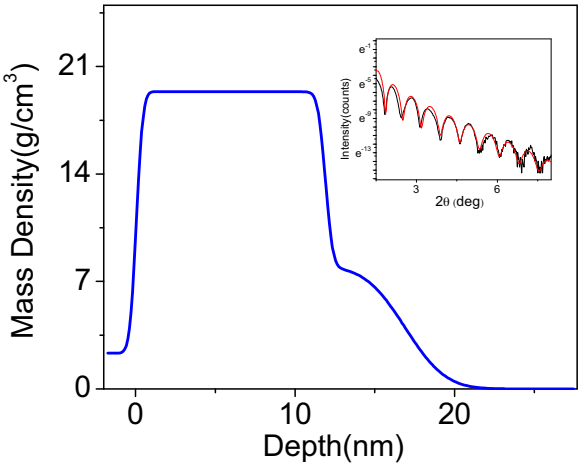

Fig. 3. Mass density profile of the WFH sample, as obtained from fitting the XRR data (shown in the inset). The depth in the mass density profile is counted from the Si substrate towards the upper layers (bottom-up).

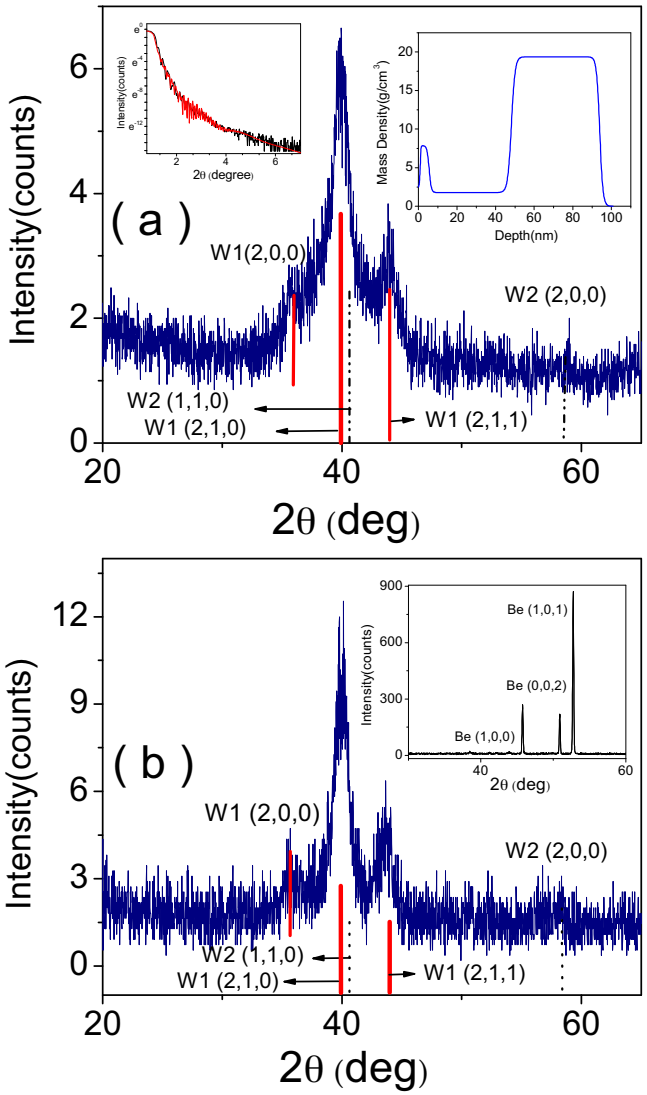

Fig. 4. GIXRD patterns of FH1BW (a) and FH1BWT (b) samples. Insets of (a) show the XRR patterns and the involved mass density profile of the FH1BW sample whereas the inset of (b) presents the GIXRD pattern of the Be target used for the deposition of the FH1BW type samples. The depth in the mass density profile is counted from the Si substrate towards the upper layers (bottom-up).

consistent acquisition time (about 20 h on each spectrum), the involved statistics remain not satisfactory for a precise Rietveld analysis of the GIXRD data. However, in case of sample FH1BW, clearly appeared a higher relative amount of the W1 phase with respect to the W2 phase as well as very low structural coherence lengths of the tungsten crystallites (less than 10 nm, as resulting from a simple Scherrer formula with $k = 1$ and a linewidth of about 1.5° [9]). The mass density profile, as obtained by XRR data (see insets of Fig. 4(a)) stands for a geometrical structure of this sample, of type Si/Fe(≈5 nm)/Be(≈45 nm)/W(≈45 nm) with rough interfaces, especially on the Fe/Be side. Following the thermal treatment, the crystallization of the W film is improved and the relative amount of the W1 phase is increasing, as derived from a substantial narrowing of the main diffraction peaks centered around 40° and 44° (2θ), whereas the Be film still keeps its amorphous like structure. No XRR interference patterns are evidenced, in good agreement with a very high roughness of the overall multilayer.

The presence of the C 1s peaks in the XPS spectra of the WFH sample, of decreasing intensity at higher etching time, proves the expected contamination with carbon species down to a depth of a few nm into the material. The specific XPS peaks of W (both 4f and 4d) have been observed just after an etching of 5 nm (Fig. 5(a)), with binding energies suggesting the presence of WO_2, according to reference NIST values [10], which seems to be related to an oxidation process taking place in the W film just before the Fe deposition (opening to environment is required by the sputtering machine, in order to change the target).

On the other hand, the analysis of the Fe 2p XPS spectra of the same sample (see Fig. 5(b)) shows a sharp decrease of the Fe content at a 5 nm etched depth, namely, exactly where the W peaks firstly appear. However the Fe 2p XPS peaks are still present in the next 2 nm at variance to the W XPS peaks which are much weaker at depths belonging to the Fe layer, namely in the first 4 nm from the sample surface. By combining the data presented in Fig. 5, it results a sequential structure of type Si/W/Fe(≈5 nm) exhibiting a large roughness at the Fe/W interface, in agreement with the XRR data. In addition, the XPS data show that at the mentioned interface, mainly Fe atoms diffuse into the W layer and almost no diffusion of the W atoms into the bcc Fe side takes place. Looking closer at the Fe 2p XPS spectra in Fig. 5(b), it can be observed an evolution of their shapes, depending on the etching depth. By focusing on the Fe $2p_{3/2}$ peak at lower binding energy (an equivalent discussion can be done also on the higher binding energy peak, Fe $2p_{1/2}$), one may observe that just at the surface it is formed a relatively weak peak with a binding energy of about 711 eV. After etching 1 nm of material, the broad peak shifts at about 710 eV whereas at a higher etching depth (spectra at 2–4 nm) it starts to split in two superposed components, with binding energies of about 709 eV and 707 eV respectively. It is worth to mention that according to [10] the binding energy of the Fe $2p_3$ XPS peak is about 707 eV for the case of the metallic state (Fe^0) and it shifts slightly at higher binding energies by about 2 eV and 4 eV for the Fe^{2+} and Fe^{3+} states, respectively. Such a slight increase of the binding energy with the oxidation state of the cation also supports the presence of oxidized tungsten (see above mentioned shift of 2–4 eV for the tungsten oxides with respect to metallic tungsten). The experimentally observed peaks support the following depth dependent phase composition of the films: (i) a less than 1 nm thick layer of trivalent Fe oxide (Fe_2O_3) of lower mass density is formed just at the film surface, (ii) between 1 and 2 nm from surface, an Fe oxide containing both Fe^{2+} and Fe^{3+} ions is formed (most probably, magnetite), (iii) between 2 and 5 nm from surface, excepting the mixed Fe oxide, also reduced Fe is present and (iv) a low amount of mixed Fe oxide (inevitably induced by processing route) is present also at the interface with the tungsten film. The partial oxidation of both the Fe and W films is also supported by the observed O 1s XPS peaks in the spectra collected at different etching depths, as shown in Fig. 5(c). According to these data, the oxide amount decreases drastically at 5 nm etching depth, where the splitting of the peak might be related to two different species of oxides (Fe oxide and tungsten oxide, respectively).

The XPS spectra collected on the as deposited sample FH1BW at different etching depths, in the energy ranges belonging to W 4f, Be 1s and Fe 2p are shown in Fig. 6. It might be directly observed that Be signals start to be present only at depths higher than 40 nm and disappear at depths higher than 90 nm (the Si $2p_3$ signal at about 100 eV becomes evident at an etching depth of 110 nm). The binding energy of Be 1s, shifts slightly from higher values approaching 114 eV, specific to oxidized Be in the upper part of the Be film, down to lower values of about 112 eV, specific to neutral Be phase, towards the interface with the Fe layer. A same shifting trend of the binding energy versus the etching depth is also observed in the case of the W 4f peaks, indicating an enhanced oxidation of the W films, especially at the outermost layers, where the substantial large shift (more than 37 eV binding energy) indicates the presence of unusual high oxidation states of W, including WO_3 [10].

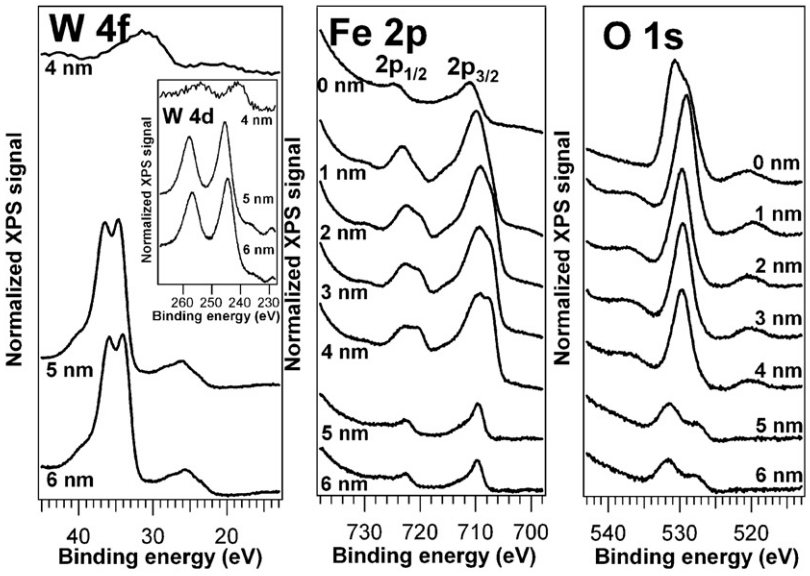

BE position of peak (eV) / Depth (nm)	W 4f$_{7/2}$	W 4d$_{5/2}$	Fe 2p$_{1/2}$		Fe 2p$_{3/2}$		O 1s$_{1/2}$	
0	-	-	724.8		711.2		530.7	529.0
1	-	-	723.3		709.9		529.0	
2	-	-	722.6	720.4	709.1	707.2	529.8	
3	-	-	722.3	720.3	709.3	707.5	529.6	
4	-	-	722.9	720.5	709.1	707.8	529.7	
5	34.6	245.7	722.4		709.7		531.5	527.6
6	34.1	244.7	722.6		709.7		531.6	527.8

Reference values (NIST):

W 4f$_{7/2}$ _____ 31.4 eV (W) / 33.4 eV (WO2) / 36.0 eV (WO_3)
W 4d$_{5/2}$ _____ 243.5 eV (W) / 247.8 eV (WO_3)
Fe 2p$_{1/2}$ _____ 723.5 eV (Fe_3O_4) / 724.0 eV (Fe_2O_3)
Fe 2p$_{3/2}$ _____ 711.4 eV (Fe_2O_3) / 709.0 eV (Fe_3O_4) / 709.9 eV (FeO) / 707.1 eV (Fe)
O 1s$_{1/2}$ _____ 529.8 eV (Fe_2O_3) / 529.7 eV (Fe_3O_4) / 531.0 eV (WO_2)

Fig. 5. XPS spectra of the WFH sample corresponding to W 4f (W 4d in inset) (a), Fe 2p (b) and O 1s (c) at different etching depths. No specific W signals were obtained at etching depth lower than 5 nm (steps of 1 nm have been considered).

At variance to the Be case, the XPS data definitely show the presence of the W atoms down to the deepest etching depth of 100 nm. Most probably, this unexpected finding has to be correlated with an enhanced top-down diffusion of the W atoms during the growth process, aspect which has to be carefully investigated in further studies. A significant presence of Fe is evidenced only at etching depth of about 100 nm and moreover, the observed binding energies (e.g. about 708 eV for the 2p3/2 XPS peak) indicate that the Fe film is mainly in its metallic state. Hence, the XPS data are in good agreement with the layered structure of the film, observed by XRR, of type Si/Fe(≈5 nm)/Be(≈45 nm)/W(≈45 nm), but also put in evidence an unexpected diffusion of the W atoms into the Be films and also an increasing oxidation of the structure, at its upper part.

The conversion electron Mössbauer (CEM) spectra collected at room temperature (RT) are shown in Fig. 7, for the following samples: WF: Si/W(10 nm)/Fe(4 nm), before the hydrogenation (a), WFH: Si/W(10 nm)/Fe(4 nm), after hydrogenation (b), F1: Si/Fe(4 nm), before the hydrogenation (c), FH1: Si/Fe(4 nm) after hydrogenation (d), FH1BW: FH1/Be(30 nm)/W(30 nm) (e) and FH1BWT: FH1/Be(30 nm)/W(30 nm) after the thermal annealing for 10 min in vacuum at 600 °C (f). The main hyperfine parameters and phase composition resulted from their fitting using the NORMOS program are given in Table 1.

The Mössbauer spectrum of the WF sample showing just a central broad paramagnetic pattern has been fitted by two central doublets, one being assigned via its hyperfine parameters, isomer shift, IS, of 0.28 mm/s and quadrupole splitting, QS, of 0.78 mm/s, to a distorted Fe^{3+} phase of superparamagnetic Fe_2O_3, and the other one, with larger isomer shift (IS = 0.65 mm/s) and quadrupole splitting (QS = 1.10 mm/s) suggesting a defected configuration around a Fe^{2+} species (atypical Fe^{2+} in defect wüstite (FeO)) [11], with electronic exchange between Fe^{2+} and Fe^{3+}. It is worth to mention that an alternative possible assignation of the paramagnetic central pattern of larger IS would be to Fe ions inside the oxidized W film (even oxidation state, e.g. +2), having in mind that the presence of an oxidized W film in sample WF is strongly supported by XPS data for hydrogenated sample WFH. However, a quite similar Mössbauer component has been also observed in sample F1, without W, providing arguments for the initial assignment to wüstite. On the other hand, for the other samples, all the further assignments of the central paramagnetic patterns to Fe^{3+} and Fe^{2+} ions in superparamagnetic Fe_2O_3 (containing only Fe^{3+}) and/or Fe_3O_4 (with both Fe^{2+}

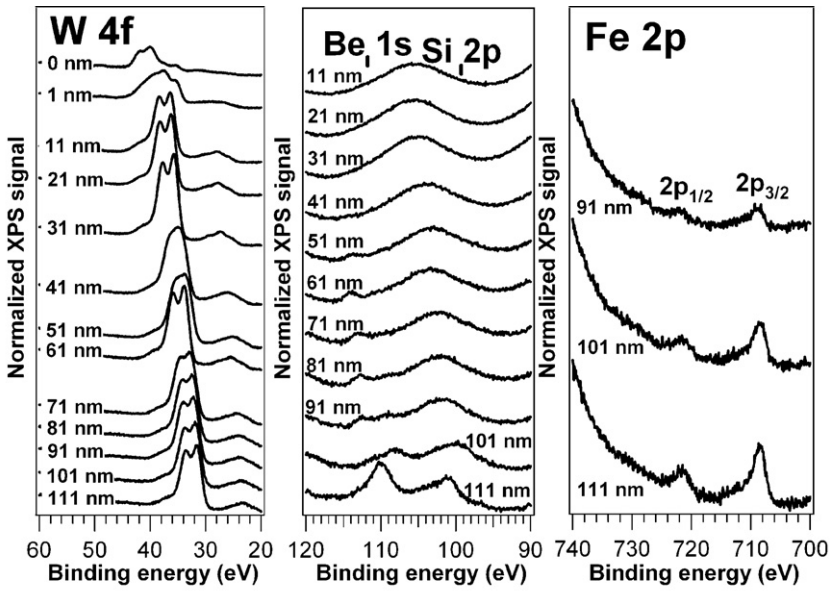

Depth (nm) \ BE position of peak (eV)	W $4f_{7/2}$	Be $1s_{1/2}$	Fe $2p_{1/2}$	Fe $2p_{3/2}$
0	40.1	-	-	-
1	37.7	-	-	-
11	36.4	-	-	-
21	36.2	-	-	-
31	35.8	-	-	-
41	35.0	-	-	-
51	33.8	113.9	-	-
61	33.8	113.8	-	-
71	33.0	113.1	-	-
81	32.5	112.7	-	-
91	32.2	112.5	722.3	709.3
101	31.9	110.8	721.6	708.7
111	31.5	110.3	721.5	708.7

Reference values (NIST):

Be $1s_{1/2}$ _____ 113.7 eV (BeO) / 111.8 eV (Be)

Fig. 6. XPS spectra of the FH1BW sample in the W 4f region (a), the Be 1s/Si 2p region (b) and the Fe 2p binding energy range (c), recorded after subsequent etching depths (steps of 10 nm have been considered).

and Fe^{3+}) oxides are supported by the Mössbauer hyperfine parameters values, XPS results, the mass density profile derived via XRR and also by extrapolating to the Fe film the very low crystallite size of the tungsten phases, the only ones observed by GIXRD in the case of sample FH1BW.

The CEM spectrum of sample WFH has been fitted by a relatively broad sextet and two central paramagnetic patterns, whose hyperfine parameters can be attributed to both Fe^{3+} and Fe^{2+} (see Table 1), giving rise to a mixture of Fe_2O_3 and Fe_3O_4 oxides. The broad sextet has been considered via a distribution of hyperfine fields, presented on the right side of each spectrum containing such a graph. By the involved hyperfine parameters (IS = 0.0 mm/s, QS = 0.0 mm/s) and the most probable hyperfine magnetic field, quite similar to the average hyperfine magnetic field, B_{hf} = 33.17 T), this component is definitely assigned to a metallic α-Fe phase. Its relative content rises up to a value of 63% (the rest of 37% belonging to the mixture of Fe_2O_3 and Fe_3O_4 oxides, with a most pronounced contribution of the former one, as suggested by the only 3% contribution of Fe^{2+}). Such results are fully consistent with the XPS data collected on this sample, providing in addition, valuable information about the detailed Fe phase content in the sample.

The CEM spectrum of sample F1 can also be handled via two components with similar hyperfine parameters as for the non hydrogenated sample WF. The two components were accordingly assigned to Fe^{3+} positions in superparamagnetic Fe_2O_3 and to the atypical Fe^{2+} of defect FeO (see Table 1). It is worth noticing at this point that Fe–Si phases giving rise to paramagnetic like central components with hyperfine parameters values close to the ones of doublet D1 in Table 1 cannot be disregarded in case of the F1 sample. In order to promote a definite support against the assignment of the doublet D1 in the Mössbauer spectrum of sample F1 to an Fe–Si phase, we will briefly analyze the CEM spectrum of sample FH1. Similar to the case of the hydrogenated sample WFH, it has been fitted by a sextet with distributed magnetic hyperfine field, assigned to metallic Fe and by two doublets (see Table 1). The first one, D1, was related to Fe^{3+} in rather strongly distorted positions belonging to a mixture of Fe_2O_3 and Fe_3O_4 oxides whereas the second, D2, to Fe^{2+} ions in Fe_3O_4. The relative content of metallic Fe in this sample is 59% and the rest of 41% belongs to Fe oxide

Table 1
Hyperfine parameters and Fe phase content in the analyzed samples.

Sample	Position/pattern	IS (mm/s)	QS (mm/s)	B_{hf} (T)	C (%)	Phase
WF	D1	0.28(1)	0.78(2)	–	86(1)	Fe^{3+} in SP Fe_2O_3
	D2	0.65(2)	1.10(6)	–	14(1)	Fe^{2+} in defect FeO
WFH	S	0.00(1)	0.00(1)	33.17(3)	63	α-Fe
	D1	0.42(1)	0.95(2)	–	34	Fe^{3+} in SP $Fe_2O_3 + Fe_3O_4$
	D2	1.10	2.40(9)	–	3	Fe^{2+} in SP Fe_3O_4
F1	D1	0.31(1)	0.66(1)		64	Fe^{3+} in SP Fe_2O_3
	D2	0.65(2)	0.94(2)		36	Fe^{2+} in defect FeO
FH1	S	0.00(1)	0.00(1)	32.93(9)	59	α-Fe
	D1	0.37(1)	1.00(3)		34	Fe^{3+} in SP $Fe_2O_3 + Fe_3O_4$
	D2	0.90(9)	2.00		7	Fe^{2+} in SP Fe_3O_4
FH1BW	S	−0.01(1)	0.00	33.07(9)	68	α-Fe
	D1	0.77(5)	0.75(9)		24	Fe^{3+} in SP $Fe_2O_3 + Fe_3O_4$
	D2	1.00(6)	2.00		8	Fe^{2+} in SP Fe_3O_4
FH1BWT	D	0.20(1)	0.52(1)		100	Fe–Be

phases (Fe_2O_3 and Fe_3O_4 seem to be in almost equal proportion of about 20% in this sample). In the case of the alternative assignment of the doublet D1 to an Fe–Si phase in both F1 and FH1 samples, the Fe content of the Fe-Si phase in FH1 sample has to be less than half from its amount in sample F1 (the rest of Fe precipitating into metallic Fe). Among the Fe-Si phases from literature giving rise to paramagnetic patterns in the Mössbauer spectrum are: metastable c-FeSi phases [12], then the amorphous and crystalline Fe_xSi_{1-x} phases with $x < 0.5$ [12 and references therein] and α-, β- and γ-$FeSi_2$ [11,13] (fortunately Fe_3Si thin films and Fe_xSi_{1-x} with $x > 0.5$ show non zero hyperfine fields in the Mössbauer spectra at room temperature [11,14]). Average quadrupole splittings of about 0.5–0.7 mm/s are compatible with most of these compounds, but their isomer shifts show peculiar behavior. In Fe_xSi_{1-x} phases with $x > 0.5$, the IS values decrease continuously with x, from about 0.27 mm/s at $x = 0.5$ down to 0.00 mm/s at $x = 1$ (pure Fe) [12]. Moreover, the isomer shift decreases by decreasing the conductive character of the films [13], e.g. from about 0.27 mm/s in conducting FeSi or α-$FeSi_2$ to 0.20 mm/s in γ-$FeSi_2$ and further to about 0.07 mm/s in the more semiconducting β-$FeSi_2$. It is useful to mention that according to [15] a similar decreasing trend has been also observed in amorphous Fe_xSi_{1-x}, namely from larger positive values for the more conductive $Fe_{0.5}Si_{0.5}$ to lower values for the more semiconducting $Fe_{0.2}Si_{0.8}$. Hence, isomer shift values at room temperature lower than 0.28 mm/s are expected for all Fe–Si compounds, with slightly lower positive values for the paramagnetic compounds with a more pronounced semiconducting behavior, expectedly induced at a higher Si relative content. Looking to the data from Table 1 (for the F1 and FH1 samples), IS values higher than 0.32 mm/s are clearly observed. Additionally, the IS value of D1 in sample FH1 is slightly higher than in sample F1, in spite of an expected Fe–Si paramagnetic phase of higher Si content (and consequently with more semiconducting behavior and lower IS) in the FH1 sample. The above mentioned disagreements eliminate the assignation of the D1 component in the Mössbauer spectra of samples F1 and FH1, to Fe–Si phases and plead for the assumption of a relatively low atomic interdiffusion at the Fe/Si interface, which will be further considered for the next two samples.

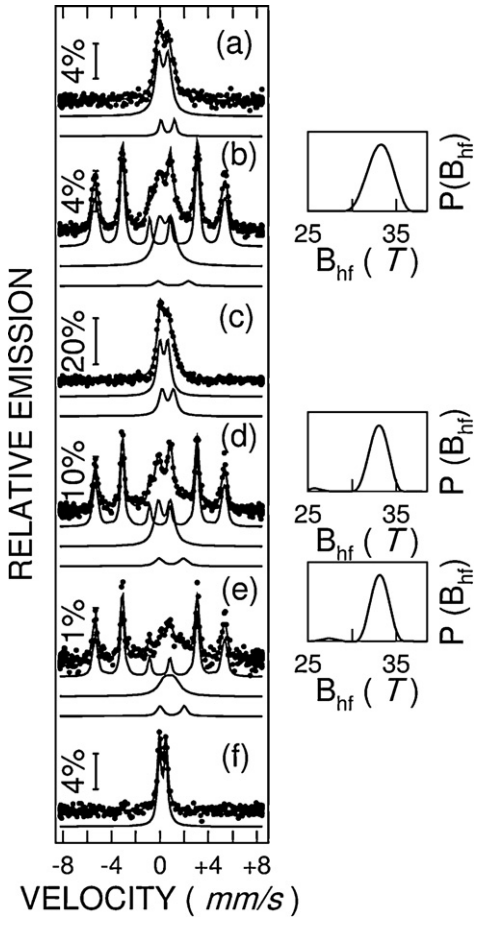

Fig. 7. CEM spectra at RT of the following samples: WF (a), WFH (b), F1 (c), FH1 (d), FH1BW (e) and FH1BWT (f). The probability distribution of hyperfine magnetic fields, fitting the sextet pattern, is shown on the right side of each corresponding spectrum.

The CEM spectrum of sample FH1BW has also evidenced the presence of the sextet assigned to metallic Fe, of a higher relative spectral contribution (relative area) than in the previous sample FH1 (68% as compared to 59%) as well as of the two doublets responding for Fe^{3+} and Fe^{2+} species (the relative amount of magnetite seems to prevail in this sample over the Fe_2O_3, within the ratio 3 to 1). Finally, the CEM spectrum of sample FH1BWT shows just a doublet with IS = 0.20 mm/s and QS = 0.52 mm/s, standing for a strong intermixing of the Fe/Be/W layered structure. While the XPS data collected on the FH1BW sample have shown a strong penetration of the W atoms close to the Fe buffer layer as well as an almost complete metallic character at the Fe/Be interface (W, Be and Fe showing typical binding energies for more metallic species), it rises up the question of the strongest diffusion at the Fe/Be interface (a sharp Si/Fe interface is assumed, based on the previously mentioned discussions whereas the presence of Fe oxides is excluded also by the involved value of IS). According to Ref. [16], slightly negative IS values (between −0.15 and −0.13 mm/s) correspond to tungsten rich Fe-W alloys, in disagreement with the positive IS value of the observed doublet, mentioned in Table 1. On the other hand, low positive IS values of about 0.17(5) mm/s are mentioned as well for Fe–Be systems (a paramagnetic phase

appears for Be concentrations exceeding 75%) [17]. Hence, the data from Table 1 are consistent with a strong diffusion of the Fe atoms inside the Be layer, induced by the thermal treatments of the Si/Fe/Be/W multilayers annealed for 10 min at 600 °C.

4. Conclusions

The investigation of multi-layer interface behavior was realized via Fe buffer layers enriched in the ^{57}Fe Mössbauer isotope grown directly on Si(0 0 1) substrates or on thin W underlayers. A partial reduction of the films has been obtained via their subsequent treatment in hydrogen atmosphere. Be(30 nm)/W(30 nm) bilayers have been grown on the hydrogenated Fe tracer layers, via a thermionic vacuum arc method and a thermal treatment, performed in vacuum, at 600 °C for 10 min was subsequently applied. All structures appearing in various processing stages, have been characterized with respect to morphological–structural, phase composition and diffusion aspects, via AFM, GIXRD, XRR, XPS and CEMS.

The gradual investigation of the processed samples has provided relevant information. The surface roughness of the as grown Si/Fe/Be/W structure increases drastically as compared to the roughness of the initial hydrogenated Si/Fe structure. Annealing treatments induced an even higher roughness of the structure, with large and deep craters, proving that the Be underlayer has a negative influence on the quality/density/adherence of the upper W layer. Excepting the about 40 nm thick W layer, all the other involved layers of the analyzed structures have shown a poor crystallization and almost short range order. Two W phases have been evidenced by GIXRD in the Si/Fe/Be/W system, their relative content depending on the annealing conditions. However, their coherence length is very low (nm range) suggesting that the coherence lengths and crystallization degree have to be even lower for the rest of the structure components. XPS data are consistent with a high surface oxidation, even for the hydrogenated systems, where a higher reduction of the elements is observed mainly in the deeper layers. A strong diffusion of the W atoms into the Be layer is observed for the as prepared Si/Fe/B/W system, where Mössbauer spectra are consistent with a sharp Fe/Si interface and the presence of still oxidized Fe superparamagnetic phases (mainly magnetite) along the Fe film. At variance, annealing treatments remove the oxygen from the Fe/Be interface, but induce a strong diffusion of the Fe atoms into the Be layer.

Acknowledgements

The financial support through the Romanian National Program IDEI, project number PN2-IDEI 1382/2008 and project number BS-M-5-EUROATOM is highly acknowledged.

References

[1] S.J. Zinkle, Fusion Eng. Des. 74 (2005) 31–40.
[2] E.E. Bloom, S.J. Zinkle, F.W. Wiffen, J. Nuclear Mater. 329–333 (2004) 12–19.
[3] Fusion News, Newsletter, vol. 3, 2009, ISSN 1818-5355.
[4] C.P. Lungu, I. Mustata, G. Musa, V. Zaroschi, A.M. Lungu, K. Iwasaki, Vacuum 76 (2004) 127.
[5] V. Kuncser, I. Mustata, C.P. Lungu, A.M. Lungu, V. Zaroschi, W. Keune, B. Sahoo, F. Stromberg, M. Walterfang, L. Ion, G. Filoti, Surf. Coat. Technol. 200 (2005) 980.
[6] V. Kuncser, G. Schinteie, P. Palade, I. Jepu, I. Mustata, C.P. Lungu, F. Miculescu, G. Filoti, J. Alloys Compd. 499 (2010) 23–29.
[7] R.A. Brand, Nuclear Instrum. Method Phys. Res. B 28 (1987) 398.
[8] V. Kuncser, F. Tolea, G. Schinteie, I. Jepu, P. Palade, Digest J. Nanomater. Biostruct. 6 (1) (2011) 199–206.
[9] C. Suryanarayana, M. Grant Norton, X-ray Diffraction; A Practical Approach, Plenum Press, New York, 1998.
[10] http://srdata.nist.gov/xps/selEnergyType.aspx; http://www.lasurface.com/database/spectrexps.php.
[11] N.N. Greenwood, T.C. Gibb, Mössbauer Spectroscopy, Chapmann and Hall, London, 1971.
[12] M. Walterfang, W. Keune, K. Trunov, R. Peters, U. Rucker, K. Westerholt, Phys. Rev. B 73 (2006) 214423.
[13] J. Desimoni, F.H. Sanchez, M.B. Fernandez van Raap, H. Bernas, C. Clerc, X.W. Lin, Phys. Rev. B 51 (1) (1995) 86–90.
[14] K. Trunov, M. Walterfang, W. Keune, N.K. Utochkina, A. Trunova, Thin Solid Films 516 (2008) 6205–6209.
[15] F.H. Sanchez, M.B. Fernandez van Raap, J. Desimoni, Phys. Rev. B 44 (1991) 4290.
[16] G. Le Caer, P. Delcroix, T.D. Shen, B. Malaman, Phys. Rev. B 54 (18) (1996) 12775–12786.
[17] O. Keizo, J. Appl. Phys. 39 (4) (1968) 2123–2126.